X-ray free-electron laser induced acoustic microscopy (XFELAM)

Seongwook Choi [a],[1], Sinyoung Park [a],[1], Jiwoong Kim [a], Hyunhee Kim [a], Seonghee Cho [a], Sunam Kim [b], Jaeku Park [b], Chulhong Kim [a],[*]

[a] *Pohang University of Science and Technology (POSTECH), Medical Device Innovation Center, Department of Electrical Engineering, Convergence IT Engineering, Mechanical Engineering, Medical Science and Engineering, 77 Cheongam-ro, Pohang 37673, Republic of Korea*
[b] *Pohang Accelerator Laboratory, 77 Cheongam-ro, Pohang 37673, Republic of Korea*

ABSTRACT

The X-ray free-electron laser (XFEL) has remarkably advanced X-ray imaging technology and enabled important scientific achievements. The XFEL's extremely high power, short pulse width, low emittance, and high coherence make possible such diverse imaging techniques as absorption/emission spectroscopy, diffraction imaging, and scattering imaging. Here, we demonstrate a novel XFEL-based imaging modality that uses the X-ray induced acoustic (XA) effect, which we call X-ray free-electron laser induced acoustic microscopy (XFELAM). Initially, we verified the XA effect by detecting XA signals from various materials, then we validated the experimental results with simulation outcomes. Next, in resolution experiments, we successfully imaged a patterned tungsten target with drilled various-sized circles at a spatial resolution of 7.8 ± 5.1 μm, which is the first micron-scale resolution achieved by XA imaging. Our results suggest that the novel XFELAM can expand the usability of XFEL in various areas of fundamental scientific research.

1. Introduction

Since the X-ray was first discovered in 1895, its high transmittance and directivity have revolutionized imaging technology, enabling applications such as X-ray computed tomography, scanning transmission X-ray microscopy, and ptychography) [1]. To achieve better resolution and sensitivity in X-ray-based imaging, significant efforts have been made to develop brighter synchrotron radiation sources. The X-ray free-electron laser (XFEL), introduced in 2009, uses the principle of self-amplified spontaneous emission (SASE) to replace the previous 3rd generation synchrotron's storage ring [2,3]. The XFEL can generate X-rays with an extremely short pulse width of 1–100 fs and more than 100 million times the peak power intensity of previous synchrotrons [1]. SASE also produces an X-ray beam to have low emittance and high coherence [1]. Further, because the 3rd generation synchrotron X-ray beam can damage the target, it is used at cryogenic temperatures. In contrast, the ultrashort pulse width of XFEL, measured in femtoseconds, can probe a target before it is destroyed [4–6]. X-ray techniques, such as X-ray absorption/emission spectroscopy, diffraction imaging, and scattering imaging have made significant advances by taking advantage of the excellent properties of XFEL [1]. X-ray absorption spectroscopy can

capture the excitation of electrons from the ground state to the core-excited state. X-ray emission spectroscopy captures relaxation processes, such as fluorescence emission of core-excited states. These methods synergistically support each other [1]. X-ray diffraction explores the structural information of atoms, molecules, and bio-composites in solid samples. When an X-ray beam passes through a target, it interacts with scattering and diffraction by atoms in its path. The resulting diffraction pattern is determined by the position, arrangement, and components of the target's crystalline structure, and can be described through the Bragg's equation [7]. X-ray scattering imaging proves particularly valuable for acquiring structural information about aperiodic and amorphous samples or proteins in solution. The analysis focuses on the interaction between the electron distribution and X-rays [8]. While this method sacrifices spatial resolution compared to diffraction crystallography, it compensates by observing larger-scale dynamics within a broader field-of-view [9]. Consequently, diffraction crystallography and scattering imaging methods complement each other, providing comprehensive structural and dynamic insights ranging from the atomic level to the macromolecular level [5,10–14]. Because of its outstanding performance, XFEL radiation is being used in a wide range of applications, from basic research in physics, the life sciences,

---

and chemistry, to industrial and applied science.

X-ray-induced acoustic imaging (XAI) has recently received great attention as a novel X-ray biomedical imaging modality that takes advantage of low-dose 3D X-ray imaging and real-time 3D dosimetry capabilities [15–28]. The X-ray-induced acoustic (XA) effect occurs when an X-ray pulse is projected into a target. The target absorbs the X-ray energy, subsequently converting it into heat energy. The heated material expands thermoelastically, creating an initial pressure wave that propagates acoustically in all directions. The initial pressures of these XA waves can be expressed as follows:

$$p_0 = \frac{\beta \eta_{th} A_e}{\rho C_V \kappa}, \tag{1}$$

where β denotes the thermal coefficient of volume expansion, η_{th} denotes the percentage of absorbed light converted into heat, A_e denotes the specific energy deposition, ρ is the density, C_V is the specific heat capacity at constant volume, and κ is the isothermal compressibility [29–33]. The omnidirectionally propagated XA waves are detected by conventional ultrasound (US) transducers. Therefore, XAI is related to X-ray absorption spectroscopy, which captures non-radiative relaxation, and is unlike X-ray emission spectroscopy, which captures fluorescence emissions as radiative relaxation [1,34]. Further, XAI can provide 3D X-ray absorption contrast information by detecting time-resolved US signals with only a single X-ray pulse.

XAI modalities have been developed in two major implementations: one is X-ray-induced acoustic computed tomography (XACT), and the other is XAI based on point-by-point detection. The former mode typically uses a multi-element US transducer array and an image-reconstruction process. The spatial resolution of XACT is mainly determined by the X-ray pulse width and is also affected by the US detector's specifications (e.g., aperture size, center frequency, and bandwidth). To generate an effective XA signal, the pulse width of the X-ray should be less than the thermal and stress confinement times [35–37]. The required pulse width can be written as

$$\tau < \tau_{th} = \frac{d_c^2}{4D_T} \tag{2}$$

and

$$\tau < \tau_{st} = \frac{d_c}{v_s}, \tag{3}$$

where τ denotes the pulse width of the X-ray, τ_{th} denotes the thermal confinement threshold, d_c is the desired spatial resolution, D_T is the thermal diffusivity, τ_{st} is the stress confinement threshold, and v_s is the speed of sound. For a 10 μm spatial resolution, the thermal confinement time and stress confinement time should be 1.8 ms and 6.7 ns, respectively [35]. Previously, Zhang et al. performed 2D real-time monitoring of radiotherapy with a spatial resolution of 1.1 mm, using a phased US transducer array with a bandwidth of 1–4 MHz and an X-ray pulse width of 4 μs [16]. Lee et al. performed 3D XACT imaging with a spatial resolution of 1.1 mm, using an arc-shaped US transducer array with a center frequency of 1 MHz and an X-ray pulse width of 50 ns [20]. Choi et al. successfully volumetrically imaged the gastrointestinal structure of a sacrificed mouse, using a conventional X-ray contrast agent (i.e., Gastrografin) [23]. Tang et al. obtained an XACT image of lead sheets with a spatial resolution of 138 μm, using a ring US transducer array with a center frequency of 5 MHz and an X-ray pulse width of 60 ns, which can be considered the best resolution among all previous XAI techniques [38]. Using the above-mentioned pulse widths, none of the XACT techniques has provided a spatial resolution better than tens of micrometres, either empirically or theoretically [39].

The latter mode, which is based on point-by-point detection, acquires XA signals with a single-element US transducer and raster scanning [40, 41]. In this implementation, the lateral spatial resolution is determined by either the X-ray beam or the acoustic focal spot, whichever is smaller.

The axial spatial resolution is still decided by the US parameters. The spatial resolutions in previous studies using this point-by-point detection method range from a few hundreds of micrometres to a couple of millimetres [21,42–45]. These resolutions are mainly limited by the difficulty of X-ray beam focusing, insufficient X-ray fluence, and/or an improper X-ray pulse repetition rate (PRR). When using a medical linear accelerator (LINAC) or a portable X-ray source as an excitation source, it is difficult to apply X-ray focusing techniques, such as using a Kirkpatrick-Baez mirror and capillary lens. Instead of implementing X-ray beam focusing, when illuminating the only small region of target with the chopped X-ray beam, no XA signal could be obtained due to insufficient X-ray fluence and consequent poor signal-to-noise ratios (SNRs). To overcome these problems, our group used a synchrotron (PLS-II, Republic of Korea) which has a relatively intense X-ray beam [21,43]. However, in that study, we were not able to separate the time-resolved XA signals because the 500-MHz PRR of the X-ray source was too fast, i.e., it was shorter than the acoustic propagation time in the medium. Here, overcoming all these limitations, we present a new XFEL configuration that achieves micrometre-level spatial resolution in XAI for the first time [39]. We used a hard XFEL at the Pohang Accelerator Laboratory (PAL-XFEL) in the Republic of Korea, which is only the third hard XFEL in the world [46]. It includes a 10-GeV S-band LINAC with a wavelength of 0.1 nm, an electron energy of 10 GeV, a PRR of 60 Hz, and 20 planar-type undulators with an undulator period of 26 mm and a minimum gap of 9.0 mm [47]. Recently, PAL-XFEL presented a self-seeded XFEL, whose peak spectral brightness is 40 times higher than that of conventional SASE [48].

Using this cutting-edge facility, PAL-XFEL, we detected XA signals induced by the XFEL for the first time. We compared the time-resolved XA signals of various materials (e.g., water, lead, tungsten, and SK3 steel) and compared those data with simulation results based on the theoretical X-ray-induced acoustic formula [43,49]. In a subsequent set of experiments, we performed 3D XFEL-induced acoustic microscopy (XFELAM) with a point-by-point detection scheme and achieved the first micrometre-level spatial resolution (7.8 ± 5.1 μm). We expect that our novel approach can be utilized to obtain X-ray absorption contrast by capturing non-radiative relaxation, and that it can complement conventional XFEL functions.

2. Materials and methods

2.1. XFEL induced acoustic microscopy

We utilized the hard XFEL at the PAL-XFEL in the Republic of Korea as an XA excitation source. Electrons with an energy of 10 GeV are accelerated by a LINAC, converted into radiation light through a hard X-ray undulator and optical hutch, and delivered to an X-ray scattering and spectroscopy-femtosecond X-ray scattering (XSS-FXS) beamline end station. Our experiments used an electron energy of 8.51—8.52 GeV and a bunch charge of 165.4—173.6 pC. The radiation beam had a photon energy of 9.75 keV and a pulse duration of ~25 fs, with a PRR of 60 Hz. These parameters were much more suitable for XAI than those in the previous studies [43] because the pulse duration is short enough for the thermal and stress confinement times and the PRR is low enough for the generated XA waves to propagate in the medium until detected. To investigate the feasibility of beam focusing, we used two pink beam modes (~10^{11} photons per pulse): a focused beam with a size of 10 μm × 10 μm, created using a beryllium compound refractive lens (Be-CRL), and an unfocused beam with a size of 300 μm × 300 μm, without a Be-CRL lens. Note that the pink beam in X-ray applications refers to a type of synchrotron radiation that is partially monochromatized, offering a balance between the high flux of a polychromatic beam and the energy specificity of a monochromatic beam.

Fig. 1 shows a schematic of the XFEL-induced acoustic microscopy (XFELAM) system. As shown in the magnified schematic in the lower right corner, we prepared an acryl water tank with a drilled circular hole
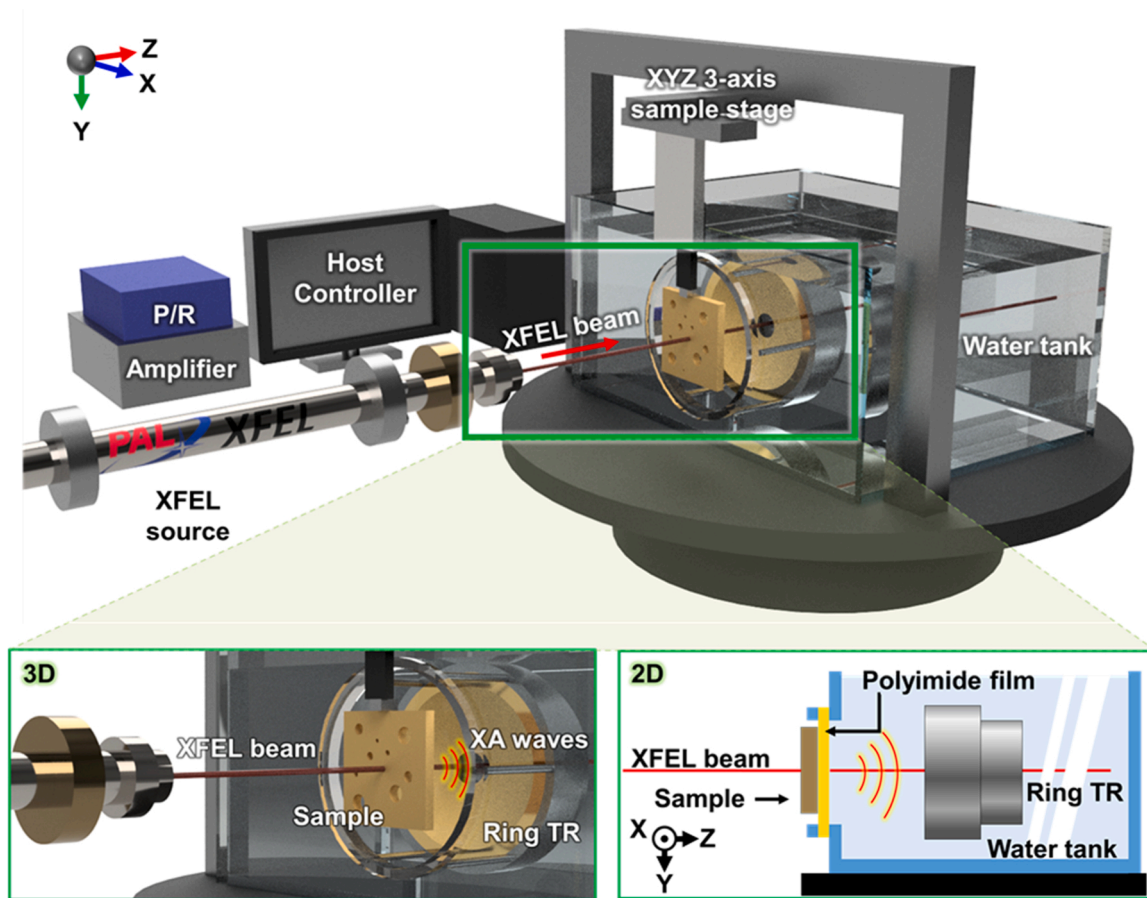
Fig. 1. Schematic of XFEL induced acoustic microscopy (XFELAM) and experimental settings. XFEL, X-ray free-electron laser; P/R, pulser/receiver; XA, X-ray-induced acoustic and TR, transducer.

in one side, then sealed the hole with a polyimide film (Kapton, Dupont, USA) for an X-ray window, chosen because polyimide is transparent to X-rays. The X-ray beam travelled from left to right, moving through the window and toward the water tank. A sample was placed on the left outer surface of the film, which is exposed to the air. The interface between the sample and polyimide film was filled with US gel (Ecosonic, Sanipia, USA) to match the acoustic impedance. When the X-ray beam irradiated the target, the generated XA waves passed through the polyimide film and water medium and were transmitted to a US transducer. We customized a single ring-shaped concave US transducer to prevent it from being destroyed by the high-power X-ray beam. The diameter of the US transducer was 32 mm, the diameter of the central hole was 5.35 mm, the center frequency was 9.1 MHz with a − 6 dB bandwidth of 52.1%, and the focal length was 26 mm. A pulser-receiver (P/R, 5072PR, Olympus NDT, USA) was used to acquire and amplify the XA signals. An amplifier (SR560, Stanford Research Systems, USA) further strengthened the signals by filtering. A high-speed digitizer (PXIe-5160, National Instruments, USA) with a maximum sampling rate of 1.25 GS/s was used for fast and accurate data acquisition. The sample was mounted on a three-axis motorized linear stage (XA05A, Kohzu Precision, Japan) that moved it for raster scanning. The host controller installed in the PAL-XFEL managed the overall operations, including increasing or decreasing the attenuator level, scanning code, and synchronizing the system with the PAL-XFEL trigger.

2.2. XA acoustic simulation

Eq. (1) was used to simulate our experimental results. The initial pressure rises of each material were calculated based on the parameters in Supplementary Table S1. Note that it was assumed that the energy depositions of each material were identical. As mentioned, the PAL-XFEL provides the brightest X-ray beam to date, and the radiation power at 0.1 nm is extremely high, as much as 30 GW. Such a high fluence and relatively high absorption coefficient cause saturation of the multiphoton/multistep absorption [50]. In this case, the difference in energy deposition among the samples can be considered negligible. We quantified the transmittance of the initial XA pressure from each sample to the US transducer by the relationship between each layer's acoustic impedance and thickness. The complex acoustic input impedance of each material, Z_{in}, can be calculated with the following equation:

$$Z_{in} = jZ_1 \frac{Z_2 + jZ_1\tan\frac{2\pi f}{c}l}{Z_1 + jZ_2\tan\frac{2\pi f}{c}l} \qquad (4)$$

where j denotes the square root of -1, Z_1 denotes the acoustic impedance of the propagation medium, Z_2 denotes the acoustic impedance of target medium, f denotes frequency, c denotes acoustic velocity, and l denotes the propagation length of the medium. A frequency of 0 to 20 MHz was employed in the simulation to calculate the propagation signal. In the frequency domain, a steady state solution was obtained by applying the reflection-to-transmission ratio based on the impedance calculated above for each frequency component, then converted into the time domain. The simulation result was processed by applying a band-pass filter to the signal, according to the transducer specifications and gains.

2.3. Experimental procedure

A sample (lead, tungsten, or SK3 steel) was attached to the polyimide film, with water on the opposite side, and US gel was applied between

the sample and the polyimide film (Fig. 1-right bottom). For the water sample case, nothing was adhered to the polyimide film. The customized ring-shaped transducer (Fig. 1) was positioned at the US focus by performing a pulse/echo test. The desired time point of the peak US echo was 34.6 μs, which is approximately the focal length of 26 mm divided by the speed of sound underwater (1500 m/s) and doubled to account for the round trip. After placing the transducer at the US focus, we then set the P/R and the amplifier in receive-mode. To amplify the XA signals, we set a P/R gain of 40 dB and an amplifier gain of 50 times.

To check the pathway of the X-ray beam, we used a disk-shaped yttrium aluminum garnet crystal doped with cerium (YAG:Ce). The YAG:Ce crystal emits visible or near-infrared light when exposed to X-rays, so it is used as a scintillator to detect X-rays. The alignment between the X-rays, sample, and US transducer was confirmed by the scintillating light. Because PAL-XFEL provides labels for each X-ray pulse specification, XA-signal normalization could be performed according to beam intensity through off-line processing. To check the reliability of the measured data, we divided a total of 60 data for each material into 6 groups of 10 and obtained the mean and standard deviation of the peak signal for each material.

During XFELAM imaging, the sample was scanned by means of an XYZ 3-axis sample stage (Fig. 1). For XFELAM imaging with an unfocused X-ray beam, 30 XA signals from each pixel were averaged. The scanning step size was 150 μm, and 68 scanning steps were executed in both the X and Y directions. After acquiring the data through scanning, we noticed that two cross-sections (e.g., the 43rd and 44th lines in the Y direction) of data were missing. We filled in the volume data for these two cross-sections by interpolating across 7 voxels in the X direction. For visualization, the volume voxels were interpolated 10 times in the XYZ-axis directions, and a moving average filter with a 5×5 mask was applied.

When performing XFLEAM with a focused X-ray beam, to prevent burning or melting the tungsten sample, we attenuated the X-ray beam by passing it through a 350 μm thick silicon wafer. The XA signals were averaged 60 times, and the scanning step size was 5 μm. There were 121 steps in the X direction and 134 in the Y direction. For visualization, the image pixels were interpolated 10 times in the XYZ-axis directions, and we applied a moving average filter with a 5×5 mask.

For the spatial resolution measurements, first, we fit the sigmoid function to the XA signals obtained from the boundary/edge of the sample to generate the edge spread function (ESF) of the experimental data. Then, the generated ESF was differentiated, and the result become the line spread function (LSF). The full width at half maximum of the normalized LSF was defined as the spatial resolution, which we calculated statistically with five ESFs because the XA signals fluctuated.

3. Results

3.1. XFEL-induced acoustic characteristics of various materials

To demonstrate the XA effect induced by the XFEL, we acquired XA signals from water, a 1-mm-thick lead specimen, a 1-mm-thick tungsten specimen, and a 0.2-mm-thick SK3 steel sample (DN52, DORCO, Republic of Korea). Fig. 2a shows the time-resolved XA signals of the water, tungsten, lead, and SK3 steel samples, and Fig. 2b shows the associated Hilbert-transformed data. The peak amplitudes of the Hilbert-transformed signals are plotted as the initial XA pressure in Fig. 2c, together with analytic simulation results based on the theoretical initial pressure of the XA effect. Although there is approximately 20% variation in the values for each material due to the assumption of ideal conditions, the two plots show a good correlation overall (see Eq. (1), Table S1, and Methods).

3.2. XFELAM imaging of a tungsten-water sample

To demonstrate the imaging capability of the XFELAM, we used two modes, one with an unfocused X-ray beam (300 μm × 300 μm along the X and Y axes, respectively) and the other with a focused X-ray beam (10 μm × 10 μm along X and Y axes, respectively). First, we acquired XA images of a flat tungsten sample with holes of diverse sizes (Fig. 3a). Initially, we used an unfocused X-ray beam. Fig. 3b shows an XA maximum amplitude projection (MAP) image of the tungsten-water sample. The dark background with the low XA signals is the tungsten, and the bright regions with the strong XA signals are water. This result correlates well with the sample test values in Fig. 2c. Some background areas, indicated by yellow arrows, exhibit relatively strong XA signals, which come from the US gel used for acoustic coupling. The distance-encoded and 3D rendered images (Fig. 3c-d) confirm the 3D imaging capability of the XFELAM. We measured the spatial resolution of the XFELAM with the unfocused beam. Fig. 3e is a zoomed-in image of the blue-boxed region in Fig. 3b, and the measured full width at half maximum (FWHM) of the line spread function is 408.4 ± 6.9 μm (Fig. 3f and see Methods). Then, we switched the excitation beam to the focused one and used 2D CRL focusing to achieve micrometre-level spatial resolution, acquiring the XA image of the red-boxed region in Fig. 3b. For comparison, Fig. 3g-h show XA images acquired with XFELAM using unfocused and focused beams, respectively. Obviously, the hole's boundary is sharply imaged with the focused beam. The spatial resolution of the focused XFELAM is quantitatively measured as 7.8 ± 5.1 μm, which represents the first achieved micrometre-level spatial resolution in XAI (Fig. 3i and see Methods).

4. Discussion and conclusion

Several imaging techniques, such as X-ray absorption/emission spectroscopy, diffraction imaging, and scattering imaging, take advantage of the XFEL's high power, short pulse width, low emissivity, and high coherence. Here, we have introduced a novel XFEL imaging modality, XFEL-induced acoustic microscopy (XFELAM). Unlike general X-ray imaging modalities, XFELAM can capture time-resolved X-ray energy deposition on a specific target, based on the non-radiative relaxation. In addition, the previously developed XAI imaging modalities
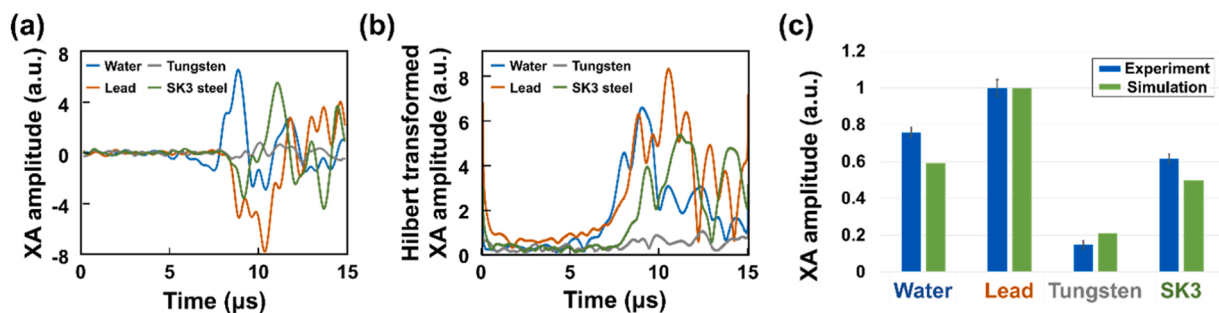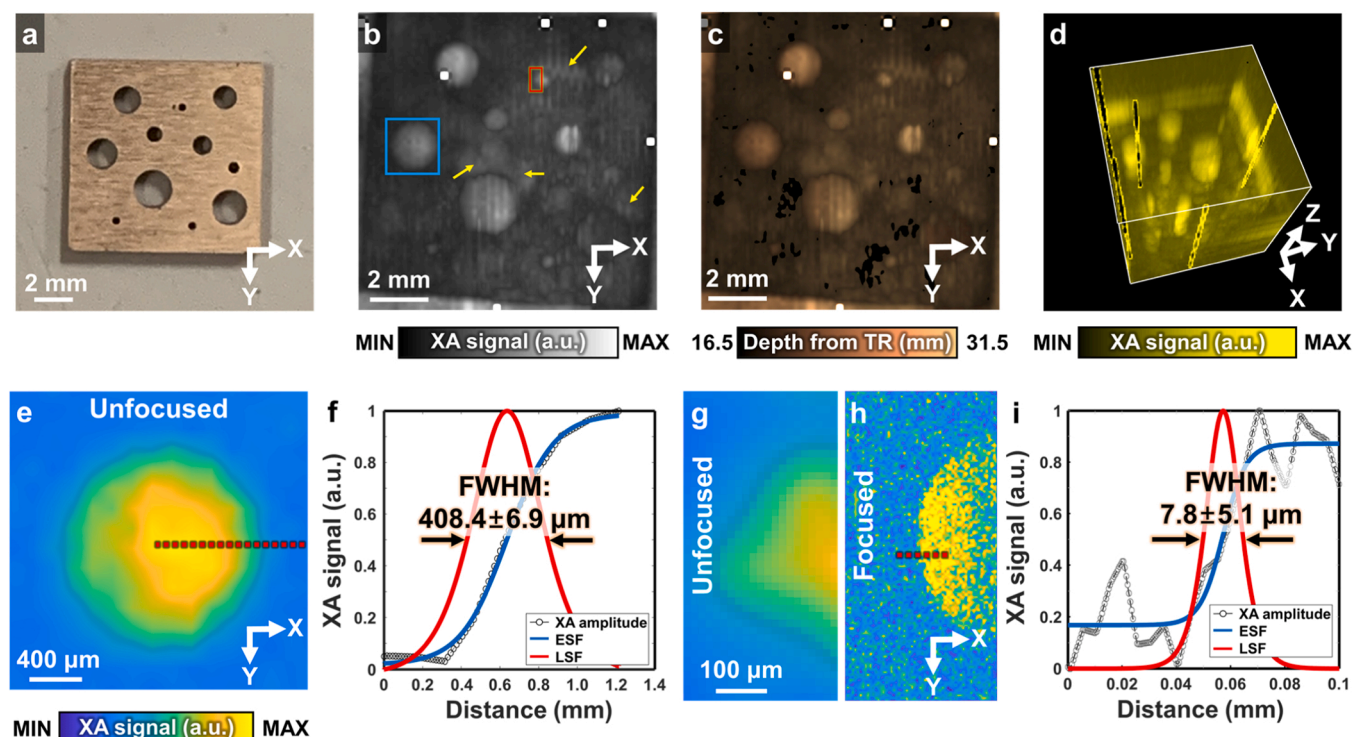

Fig. 2. XA-acoustic signals acquired from various materials: (a) raw data and (b) Hilbert transformed data. (c) Comparisons of simulated and experimental of peak XA signals from the materials. XA, X-ray-induced acoustic.

Fig. 3. (a) Photograph, (b) XA MAP image, (c) XA distance-encoded image, and (d) 3D rendered XA image of the tungsten sample, using unfocused X-ray beams. (e) Close-up XA MAP image from the blue box in (b). (f) ESF and LSF fittings from experimental XA data across the red dotted line in (e). (g) Close-up XA MAP image from the red box in (b). (h) XA MAP image of the region of (g), using focused X-ray beams. (i) ESF and LSF fittings from experimental XA data across the red dotted line in (f). XA, X-ray-induced acoustic; MAP, maximum amplitude projection; TR, ultrasound transducer; ESF, edge spread function; and LSF, line spread function.

suffer from low spatial resolution (e.g., a few hundred micrometres) due to the difficulty of focusing the X-ray beam, low signal-to-noise ratios, improper X-ray pulse widths, and/or inappropriate pulse repetition rates. Our new XFELAM achieves micrometre-level spatial resolution for the first time. We used the PAL-XFEL, which is the third established XFEL in the world. The noteworthy parameters of the PAL-XFEL are a pulse repetition rate of 60 Hz and a focused beam size of 10 μm × 10 μm, a pulse width of ~25 fs (FWHM), an electron energy of 8.5 GeV, and a photon energy of 9.75 keV. These values are much more suitable for XAI than the previously used X-ray sources. We characterized the XA effect from various materials (i.e., lead, tungsten, water, SK3 steel) by comparing experimental results with simulation results. Then, we successfully performed XFELAM imaging experiments with a tungsten-water sample, achieving a spatial resolution of 7.8 ± 5.1 μm, the first micrometre-level spatial resolution to be achieved in XAI.

The usability of this pioneering XA microscopy system could be much enhanced by a non-contact imaging configuration. First, because the XFEL's pulse width is very short, XA signals with very high frequency components may be generated. However, the current system was unable to detect intact XA signals due to the center frequency (9.1 MHz) and limited bandwidth (52.1%) of the detector, so only part of the wideband information was received. Even though the lateral resolution is a just few microns due to the small spot size of the focused x-ray beam, the system still has poor axial resolution. By using non-contact imaging techniques such as all-optical ultrasound transducer that do not require physical contact between the imaging device and the target object, broadband XA signals can be captured, and the axial resolution can be much improved [51–54]. Furthermore, we used water as a coupling medium to detect the ultrasonic signal, but the water itself generates a very strong XA signal that hinders the acquisition and analysis of XA signals from various samples. Therefore, configuring non-contact imaging by using an optical detector would allow more accurate analysis of various samples without interfering with the XA signal in water.

In the future, we believe that this technology can expand the utility of the XFEL in material science, basic medicine, and new drug development. For example, the XFEL has been used to explore shockwave phenomena from cavitation bubbles [55–58]. Those studies were interested in demonstrating the physical characteristics of shockwaves, such as their pressure. By detecting actual pressure time-resolved acoustic signals, XFELAM can provide additional information about the acoustic characteristics of shock waves. Furthermore, according to the different characteristics of crystal structures, such as single crystalline, polycrystalline, or amorphous, the XFELAM could determine physical characteristics (e.g., the thermal coefficient of volume expansion) based on the initial pressure formula of the XA effect [59]. Although the safety of human in vivo application using high-energy XFEL beam has not been verified, the unique features of XFEL show promise for studying cellular protein structures and interactions between proteins and drugs [60,61]. Although the direct medical applications of XFEL require further validation, its potential impact in the filed of structural biology and drug development is promising.

CRediT authorship contribution statement

Park Sinyoung: Conceptualization, Data curation, Methodology, Visualization, Writing – original draft, Writing – review & editing. **Kim Jiwoong:** Methodology, Resources, Validation. **Kim Hyunhee:** Methodology, Validation. **Park Jaeku:** Methodology, Resources, Supervision. **Kim Chulhong:** Conceptualization, Project administration, Supervision, Writing – review & editing. **Cho Seonghee:** Data curation, Software, Validation. **Kim Sunam:** Conceptualization, Methodology, Resources, Supervision. **Choi Seongwook:** Conceptualization, Data curation, Project administration, Software, Writing – original draft, Writing – review & editing.

Declaration of Competing Interest

The authors declare the following financial interests/personal relationships which may be considered as potential competing interests: C. Kim and S. Cho have financial interests in OPTICHO, which, however, did not support this work.

Data availability

Data will be made available on request.

Acknowledgements

Appendix A. Supporting information

Supplementary data associated with this article can be found in the online version at doi:10.1016/j.pacs.2024.100587.

References

[1] U. Bergmann, J. Kern, R.W. Schoenlein, P. Wernet, V.K. Yachandra, J. Yano, Using X-ray free-electron lasers for spectroscopy of molecular catalysts and metalloenzymes, Nat. Rev. Phys. 3 (4) (2021) 264–282.

[2] C. Bostedt, S. Boutet, D.M. Fritz, Z. Huang, H.J. Lee, H.T. Lemke, A. Robert, W. F. Schlotter, J.J. Turner, G.J. Williams, Linac coherent light source: The first five years, Rev. Mod. Phys. 88 (1) (2016) 015007.

[3] P. Emma, R. Akre, J. Arthur, R. Bionta, C. Bostedt, J. Bozek, A. Brachmann, P. Bucksbaum, R. Coffee, F.-J. Decker, First lasing and operation of an ångstrom-wavelength free-electron laser, Nat. Photonics 4 (9) (2010) 641–647.

[4] E.F. Garman, Radiation damage in macromolecular crystallography: what is it and why should we care? Acta Crystallogr. Sect. D: Biol. Crystallogr. 66 (4) (2010) 339–351.

[5] J. Kern, R. Alonso-Mori, R. Tran, J. Hattne, R.J. Gildea, N. Echols, C. Glöckner, J. Hellmich, H. Laksmono, R.G. Sierra, Simultaneous femtosecond X-ray spectroscopy and diffraction of photosystem II at room temperature, Science 340 (6131) (2013) 491–495.

[6] R. Alonso-Mori, J. Kern, R.J. Gildea, D. Sokaras, T.-C. Weng, B. Lassalle-Kaiser, R. Tran, J. Hattne, H. Laksmono, J. Hellmich, Energy-dispersive X-ray emission spectroscopy using an X-ray free-electron laser in a shot-by-shot mode, Proc. Natl. Acad. Sci. 109 (47) (2012) 19103–19107.

[7] H. Liu, J.C. Spence, XFEL data analysis for structural biology, Quant. Biol. 4 (3) (2016) 159–176.

[8] L.A. Dadinova, Y.M. Chesnokov, R.A. Kamyshinsky, I.A. Orlov, M.V. Petoukhov, A. A. Mozhaev, E.Y. Soshinskaya, V.N. Lazarev, V.A. Manuvera, A.S. Orekhov, Protective Dps–DNA co-crystallization in stressed cells: an in vitro structural study by small-angle X-ray scattering and cryo-electron tomography, FEBS Lett. 593 (12) (2019) 1360–1371.

[9] M. Levantino, B.A. Yorke, D.C. Monteiro, M. Cammarata, A.R. Pearson, Using synchrotrons and XFELs for time-resolved X-ray crystallography and solution scattering experiments on biomolecules, Curr. Opin. Struct. Biol. 35 (2015) 41–48.

[10] I. Vartanyants, I. Robinson, I. McNulty, C. David, P. Wochner, T. Tschentscher, Coherent X-ray scattering and lensless imaging at the European XFEL Facility, J. Synchrotron Radiat. 14 (6) (2007) 453–470.

[11] K.K. Patra, I. Eliah Dawod, A.V. Martin, T.L. Greaves, D. Persson, C. Caleman, N. Timneanu, Ultrafast dynamics and scattering of protic ionic liquids induced by XFEL pulses, J. Synchrotron Radiat. 28 (5) (2021).

[12] D.A. Jacques, J. Trewhella, Small-angle scattering for structural biology—Expanding the frontier while avoiding the pitfalls, Protein Sci. 19 (4) (2010) 642–657.

[13] M. Ibrahim, T. Fransson, R. Chatterjee, M.H. Cheah, R. Hussein, L. Lassalle, K. D. Sutherlin, I.D. Young, F.D. Fuller, S. Gul, Untangling the sequence of events during the S2→ S3 transition in photosystem II and implications for the water oxidation mechanism, Proc. Natl. Acad. Sci. 117 (23) (2020) 12624–12635.

[14] K. Haldrup, W. Gawelda, R. Abela, R. Alonso-Mori, U. Bergmann, A. Bordage, M. Cammarata, S.E. Canton, A.O. Dohn, T.B. van Driel, Observing solvation dynamics with simultaneous femtosecond X-ray emission spectroscopy and X-ray scattering, J. Phys. Chem. B 120 (6) (2016) 1158–1168.

[15] Y. Li, P. Samant, S. Wang, A. Behrooz, D. Li, L. Xiang, 3-D X-Ray-Induced Acoustic Computed Tomography With a Spherical Array: A Simulation Study on Bone Imaging, IEEE Trans. Ultrason., Ferroelectr., Freq. Control 67 (8) (2020) 1613–1619.

[16] W. Zhang, I. Oraiqat, H. Lei, P.L. Carson, I. El Naqa, X. Wang, Dual-Modality X-Ray-Induced Radiation Acoustic and Ultrasound Imaging for Real-Time Monitoring of Radiotherapy, BME Front. 2020 (2020).

[17] S. Choi, D. Lee, E.-Y. Park, J.-J. Min, C. Lee, C. Kim, 3D x-ray induced acoustic computed tomography: a phantom study, Photons Plus Ultrasound: Imaging and Sensing 2020, International Society for Optics and Photonics, 2020, p. 112404R.

[18] F. Forghani, A. Mahl, T.J. Patton, B.L. Jones, M.A. Borden, D.C. Westerly, C. Altunbas, M. Miften, D.H. Thomas, Simulation of x-ray-induced acoustic imaging for absolute dosimetry: Accuracy of image reconstruction methods, Med. Phys. 47 (3) (2020) 1280–1290.

[19] E. Robertson, P. Samant, S. Wang, T. Tran, X. Ji, L. Xiang, X-ray-induced acoustic computed tomography (XACT): initial experiment on bone sample, IEEE Trans. Ultrason., Ferroelectr., Freq. Control (2020).

[20] D. Lee, E.-Y. Park, S. Choi, H. Kim, J.-j Min, C. Lee, C. Kim, GPU-accelerated 3D volumetric X-ray-induced acoustic computed tomography, Biomed. Opt. Express 11 (2) (2020) 752–761.

[21] S. Choi, E.-Y. Park, S. Park, J.H. Kim, C. Kim, X-ray induced acoustic imaging using a synchrotron, Photons Ultrasound.: Imaging Sens. 2021, Int. Soc. Opt. Photonics (2021) 116423T.

[22] P. Samant, L. Trevisi, X. Ji, L. Xiang, X-ray induced acoustic computed tomography, Photoacoustics 19 (2020) 100177.

[23] S. Choi, S. Park, A. Pyo, D.-Y. Kim, J.-J. Min, C. Lee, C. Kim, In situ x-ray-induced acoustic computed tomography with a contrast agent: a proof of concept, Opt. Lett. 47 (1) (2022) 90–93.

[24] W. Choi, B. Park, S. Choi, D. Oh, J. Kim, C. Kim, Recent advances in contrast-enhanced photoacoustic imaging: overcoming the physical and practical challenges, Chem. Rev. (2023).

[25] J. Yang, S. Choi, J. Kim, B. Park, C. Kim, Recent advances in deep-learning-enhanced photoacoustic imaging, Adv. Photonics Nexus 2 (5) (2023), 054001-054001.

[26] S. Choi, J. Yang, S.Y. Lee, J. Kim, J. Lee, W.J. Kim, S. Lee, C. Kim, Deep learning enhances multiparametric dynamic volumetric photoacoustic computed tomography in vivo (DL-PACT), Adv. Sci. 10 (1) (2023) 2202089.

[27] J.-S. Wi, J. Kim, M.Y. Kim, S. Choi, H.J. Jung, C. Kim, H.-K. Na, Theoretical and experimental comparison of the performance of gold, titanium, and platinum nanodiscs as contrast agents for photoacoustic imaging, RSC Adv. 13 (14) (2023) 9441–9447.

[28] D. Oh, D. Lee, J. Heo, J. Kweon, U. Yong, J. Jang, Y.J. Ahn, C. Kim, Contrast agent-free 3D Renal ultrafast doppler imaging reveals vascular dysfunction in acute and diabetic kidney diseases, Adv. Sci. 10 (36) (2023) 2303966.

[29] L.V. Wang, H.-i Wu, Biomedical Optics: Principles and Imaging, John Wiley & Sons, 2012.

[30] C. Lee, S. Cho, D. Lee, J. Lee, J.-I. Park, H.-J. Kim, S.H. Park, W. Choi, U. Kim, C. Kim, Panoramic volumetric clinical handheld photoacoustic and ultrasound imaging, Photoacoustics 31 (2023) 100512.

[31] J. Ahn, J.W. Baik, D. Kim, K. Choi, S. Lee, S.-M. Park, J.Y. Kim, S.H. Nam, C. Kim, In vivo photoacoustic monitoring of vasoconstriction induced by acute hyperglycemia, Photoacoustics 30 (2023) 100485.

[32] E. Park, Y.-J. Lee, C. Kim, T.J. Eom, Azimuth mapping of fibrous tissue in linear dichroism-sensitive photoacoustic microscopy, Photoacoustics 31 (2023) 100510.

[33] J. Ahn, J.W. Baik, Y. Kim, K. Choi, J. Park, H. Kim, J.Y. Kim, H.H. Kim, S.H. Nam, C. Kim, Fully integrated photoacoustic microscopy and photoplethysmography of human in vivo, Photoacoustics (2022) 100374.

[34] L. Wang, C. Zhang, L.V. Wang, Grueneisen relaxation photoacoustic microscopy, Phys. Rev. Lett. 113 (17) (2014) 174301.

[35] J. Xia, J. Yao, L.V. Wang, Photoacoustic tomography: principles and advances, Electromagn. Waves 147 (2014) 1.

[36] M. Xu, L.V. Wang, Analytic explanation of spatial resolution related to bandwidth and detector aperture size in thermoacoustic or photoacoustic reconstruction, Phys. Rev. E 67 (5) (2003) 056605.

[37] Y. Wang, Y. Zhan, M. Tiao, J. Xia, Review of methods to improve the performance of linear array-based photoacoustic tomography, J. Innov. Opt. Health Sci. 13 (02) (2020) 2030003.

[38] S. Tang, D. Nguyen, A. Zarafshani, C. Ramseyer, B. Zheng, H. Liu, L. Xiang, X-ray-induced acoustic computed tomography with an ultrasound transducer ring-array, Appl. Phys. Lett. 110 (10) (2017) 103504.

[39] W. Xu, W. Xu, N. Bouet, J. Zhou, H. Yan, X. Huang, Y. Gao, M. Lu, M. Zalalutdinov, 2D MEMS-based multilayer Laue lens nanofocusing optics for high-resolution hard x-ray microscopy, Opt. Express 28 (12) (2020) 17660–17671.

[40] L. Xiang, B. Han, C. Carpenter, G. Pratx, Y. Kuang, L. Xing, X-ray acoustic computed tomography with pulsed x-ray beam from a medical linear accelerator, Med. Phys. 40 (1) (2013) 010701.

[41] S. Hickling, M. Hobson, I. El Naqa, Characterization of x-ray acoustic computed tomography for applications in radiotherapy dosimetry, IEEE Trans. Radiat. Plasma Med. Sci. 2 (4) (2018) 337–344.

[42] J. Kim, E.-Y. Park, Y. Jung, B.C. Kim, J.H. Kim, C.-Y. Yi, I.J. Kim, C. Kim, X-ray acoustic-based dosimetry using a focused ultrasound transducer and a medical linear accelerator, IEEE Trans. Radiat. Plasma Med. Sci. 1 (6) (2017) 534–540.

[43] S. Choi, E.-Y. Park, S. Park, J.H. Kim, C. Kim, Synchrotron X-ray induced acoustic imaging, Sci. Rep. 11 (1) (2021) 1–7.

[44] S. Hickling, H. Lei, M. Hobson, P. Léger, X. Wang, I. El Naqa, Experimental evaluation of x-ray acoustic computed tomography for radiotherapy dosimetry applications, Med. Phys. 44 (2) (2017) 608–617.

[45] L. Xiang, S. Tang, M. Ahmad, L. Xing, High resolution X-ray-induced acoustic tomography, Sci. Rep. 6 (2016) 26118.

[46] H.-S. Kang, C.-K. Min, H. Heo, C. Kim, H. Yang, G. Kim, I. Nam, S.Y. Baek, H.-J. Choi, G. Mun, Hard X-ray free-electron laser with femtosecond-scale timing jitter, Nat. Photonics 11 (11) (2017) 708–713.

[47] I.S. Ko, H.-S. Kang, H. Heo, C. Kim, G. Kim, C.-K. Min, H. Yang, S.Y. Baek, H.-J. Choi, G. Mun, Construction and commissioning of PAL-XFEL facility, Appl. Sci. 7 (5) (2017) 479.

[48] I. Nam, C.-K. Min, B. Oh, G. Kim, D. Na, Y.J. Suh, H. Yang, M.H. Cho, C. Kim, M.-J. Kim, High-brightness self-seeded X-ray free-electron laser covering the 3.5 keV to 14.6 keV range, Nat. Photonics 15 (6) (2021) 435–441.

[49] J. Yang, S. Choi, C. Kim, Practical review on photoacoustic computed tomography using curved ultrasound array transducer, Biomed. Eng. Lett. 17 (1) (2021).

[50] A. Danielli, C.P. Favazza, K. Maslov, L.V. Wang, Picosecond absorption relaxation measured with nanosecond laser photoacoustics, Appl. Phys. Lett. 97 (16) (2010) 163701.

[51] J. Bauer-Marschallinger, K. Felbermayer, T. Berer, All-optical photoacoustic projection imaging, Biomed. Opt. Express 8 (9) (2017) 3938–3951.

[52] O. Ogunlade, J.J. Connell, J.L. Huang, E. Zhang, M.F. Lythgoe, D.A. Long, P. Beard, In vivo three-dimensional photoacoustic imaging of the renal vasculature in preclinical rodent models, Am. J. Physiol. Ren. Physiol. 314 (6) (2018) F1145–F1153.

[53] T. Vu, D. Razansky, J. Yao, Listening to tissues with new light: recent technological advances in photoacoustic imaging, J. Opt. 21 (10) (2019) 103001.

[54] G. Wissmeyer, M.A. Pleitez, A. Rosenthal, V. Ntziachristos, Looking at sound: optoacoustics with all-optical ultrasound detection, Light.: Sci. Appl. 7 (1) (2018) 53.

[55] M. Vassholz, H. Hoeppe, J. Hagemann, J. Rosselló, M. Osterhoff, R. Mettin, T. Kurz, A. Schropp, F. Seiboth, C. Schroer, Pump-probe X-ray holographic imaging of laser-induced cavitation bubbles with femtosecond FEL pulses, Nat. Commun. 12 (1) (2021) 1–11.

[56] C.A. Stan, K. Motomura, G. Blaj, Y. Kumagai, Y. Li, D. You, T. Ono, A. Kalita, T. Togashi, S. Owada, The magnitude and waveform of shock waves induced by x-ray lasers in water, Appl. Sci. 10 (4) (2020) 1497.

[57] A. Schropp, R. Hoppe, V. Meier, J. Patommel, F. Seiboth, Y. Ping, D.G. Hicks, M.A. Beckwith, G.W. Collins, A. Higginbotham, Imaging shock waves in diamond with both high temporal and spatial resolution at an XFEL, Sci. Rep. 5 (1) (2015) 1–8.

[58] M.L. Grünbein, A. Gorel, L. Foucar, S. Carbajo, W. Colocho, S. Gilevich, E. Hartmann, M. Hilpert, M. Hunter, M. Kloos, Effect of X-ray free-electron laser-induced shockwaves on haemoglobin microcrystals delivered in a liquid jet, Nat. Commun. 12 (1) (2021) 1–11.

[59] B. Park, M. Han, H. Kim, J. Yoo, D.K. Oh, S. Moon, J. Ahn, H.G. Lim, I. Kim, H.H. Kim, Shear-force photoacoustic microscopy: toward super-resolution near-field imaging, Laser Photonics Rev. 16 (12) (2022) 2200296.

[60] J.W. Baik, H. Kim, M. Son, J. Choi, K.G. Kim, J.H. Baek, Y.H. Park, J. An, H.Y. Choi, S.Y. Ryu, Intraoperative label-free photoacoustic histopathology of clinical specimens, Laser Photonics Rev. 15 (10) (2021) 2100124.

[61] D. Kim, E. Park, J. Park, B. Perleberg, S. Jeon, J. Ahn, M. Ha, H.H. Kim, J.Y. Kim, C.K. Jung, An ultraviolet-transparent ultrasound transducer enables high-resolution label-free photoacoustic histopathology, Laser Photonics Rev. (2023) 2300652.

Sinyoung Park is a Ph.D. candidate in Electrical Engineering at POSTECH. He completed his B.S. in Electronic engineering at Kyungpook National University in 2019 and M.S. in POSTECH in 2021. His research interests are clinical photoacoustic tomography and medical device development using FPGA based hardware system.

Jiwoong Kim is an integrated MS/Ph.D. student at POSTECH in the Republic of Korea. He received his B.S. in Mechanical Engineering at POSTECH in 2020. His research interests are 3D biomedical imaging techniques includes photoacoustics and ultrasound.

Hyunhee Kim is a Ph.D. candidate in Convergence IT Engineering at POSTECH. She received her B.S. in Electrical Communication Engineering at Hanyang University and her M.S. in School of Interdisciplinary Bioscience and Bioengineering at POSTECH. Her research interests are to develop clinical imaging systems for ultrasound and photoacoustic diagnostic imaging.

Seonghee Cho Ph.D. is an assistant research faculty at POSTECH in the Republic of Korea. He received the Ph. D. degree in the interdisciplinary Bioscience and Bioengineering at POSTECH in 2022. His research interests are developing ultrasound transducers and imaging techniques, including high-frequency ultrasound transducers, transparent ultrasound transducers, ultrasound imaging, and photoacoustic imaging.

Seongwook Choi Ph.D. is a post-doctoral research associate at POSTECH in the Republic of Korea. He received the Ph. D. degree in the Convergence IT Engineering at POSTECH in 2023. His research interests are the development of novel biomedical imaging techniques, including photoacoustic, quantitative, and deep learning-enhanced imaging.

Dr. Sunam Kim earned his Ph.D. degree at Gwangju Institute of Science and Technology (GIST, Korea) and did post-doctoral training at RIKEN, Japan. He played a key role in initiation of femto-second pump probe x-ray diffraction instrument in PAL-XFEL in Korea. He currently is a beamline scientist of the PAL-XFEL and develops femto-second x-ray imaging technologies.

Jaeku Park Ph.D. works as a beamline scientist at Pohang Accelerator Laboratory's X-ray Free Electron Laser (PAL-XFEL). He earned his Ph.D. in applied physics from Ajou University in 2014. He contributed to building and implementing a beamline and experimental techniques for time-resolved x-ray scattering experiments for PAL-XFEL since 2015. Currently, he focuses on researching signal processing for time-resolved x-ray scattering and spectroscopy.

Prof. Chulhong Kim earned his Ph.D. degree and did post-doctoral training at Washington University in St. Louis, Missouri. He currently holds the Young Distinguished Professorship and Mueunjae Chair Professorship, and is a Professor of Convergence IT Engineering, Electrical Engineering, Mechanical Engineering, Medical Science and Engineering, and Medical Device Innovation Center at Pohang University of Science and Technology in the Republic of Korea. He has received a 2017 IEEE EMBS Early Career Achievement Award, the 2017 Korean Academy of Science and Technology Young Scientist Award, the 2016 Nightingale Award from IFMBE, and the 2017 KOSOMBE Young Investigator Award for "Contributions to multi-scale photoacoustic imaging, ranging from superresolution atomic force photoactivated microscopy for research to systems for clinical applications".